Biomedical Optics EXPRESS

Ultra-widefield retinal MHz-OCT imaging with up to 100 degrees viewing angle

Jan Philip Kolb,[1,2] Thomas Klein,[2,3] Corinna L. Kufner,[2] Wolfgang Wieser,[2,3] Aljoscha S. Neubauer,[4] and Robert Huber[1,2,*]

[1]*Institut für Biomedizinische Optik, Universität zu Lübeck, Peter-Monnik-Weg 4, 23562 Lübeck, Germany*
[2]*Lehrstuhl für BioMolekulare Optik, Fakultät für Physik, Ludwig-Maximilians-Universität München, Oettingenstr. 67, 80538 Munich, Germany*
[3]*Optores GmbH, Nymphenburger Str. 10, 80335 München, Germany*
[4]*Augenklinik der Ludwig-Maximilians-Universität München, Mathildenstraße 8, 80336 Munich, Germany*
**Robert.Huber@bmo.uni-luebeck.de*

Abstract: We evaluate strategies to maximize the field of view (FOV) of in vivo retinal OCT imaging of human eyes. Three imaging modes are tested: Single volume imaging with 85° FOV as well as with 100° and stitching of five 60° images to a 100° mosaic (measured from the nodal point). We employ a MHz-OCT system based on a 1060nm Fourier domain mode locked (FDML) laser with a depth scan rate of 1.68MHz. The high speed is essential for dense isotropic sampling of the large areas. Challenges caused by the wide FOV are discussed and solutions to most issues are presented. Detailed information on the design and characterization of our sample arm optics is given. We investigate the origin of an angle dependent signal fall-off which we observe towards larger imaging angles. It is present in our 85° and 100° single volume images, but not in the mosaic. Our results suggest that 100° FOV OCT is possible with current swept source OCT technology.

OCIS codes: (170.4500) Optical coherence tomography; (170.3880) Medical and biological imaging; (170.4460) Ophthalmic optics and devices; (120.3890) Medical optics instrumentation; (140.3510) Lasers, fiber.

References and Links

1. D. Huang, E. A. Swanson, C. P. Lin, J. S. Schuman, W. G. Stinson, W. Chang, M. R. Hee, T. Flotte, K. Gregory, C. A. Puliafito, and J. G. Fujimoto, "Optical coherence tomography," Science **254**(5035), 1178–1181 (1991).
2. A. F. Fercher, C. K. Hitzenberger, W. Drexler, G. Kamp, and H. Sattmann, "In vivo optical coherence tomography," Am. J. Ophthalmol. **116**(1), 113–114 (1993).
3. E. A. Swanson, J. A. Izatt, M. R. Hee, D. Huang, C. P. Lin, J. S. Schuman, C. A. Puliafito, and J. G. Fujimoto, "In vivo retinal imaging by optical coherence tomography," Opt. Lett. **18**(21), 1864–1866 (1993).
4. C. A. Puliafito, M. R. Hee, C. P. Lin, E. Reichel, J. S. Schuman, J. S. Duker, J. A. Izatt, E. A. Swanson, and J. G. Fujimoto, "Imaging of macular diseases with optical coherence tomography," Ophthalmology **102**(2), 217–229 (1995).
5. G. J. Tearney, M. E. Brezinski, B. E. Bouma, S. A. Boppart, C. Pitris, J. F. Southern, and J. G. Fujimoto, "In vivo endoscopic optical biopsy with optical coherence tomography," Science **276**(5321), 2037–2039 (1997).
6. A. M. Sergeev, V. M. Gelikonov, G. V. Gelikonov, F. I. Feldchtein, R. V. Kuranov, N. D. Gladkova, N. M. Shakhova, L. B. Snopova, A. V. Shakhov, I. A. Kuznetzova, A. N. Denisenko, V. V. Pochinko, Y. P. Chumakov, and O. S. Streltzova, "In vivo endoscopic OCT imaging of precancer and cancer states of human mucosa," Opt. Express **1**(13), 432–440 (1997).
7. G. J. Tearney, M. E. Brezinski, J. F. Southern, B. E. Bouma, S. A. Boppart, and J. G. Fujimoto, "Optical biopsy in human gastrointestinal tissue using optical coherence tomography," Am. J. Gastroenterol. **92**(10), 1800–1804 (1997).
8. N. Hanna, D. Saltzman, D. Mukai, Z. Chen, S. Sasse, J. Milliken, S. Guo, W. Jung, H. Colt, and M. Brenner, "Two-dimensional and 3-dimensional optical coherence tomographic imaging of the airway, lung, and pleura," J. Thorac. Cardiovasc. Surg. **129**(3), 615–622 (2005).
9. J. M. Schmitt, M. J. Yadlowsky, and R. F. Bonner, "Subsurface imaging of living skin with optical coherence microscopy," Dermatology (Basel) **191**(2), 93–98 (1995).
10. B. W. Colston, U. S. Sathyam, L. B. Dasilva, M. J. Everett, P. Stroeve, and L. L. Otis, "Dental OCT," Opt. Express **3**(6), 230–238 (1998).

#232125 - $15.00 USD Received 7 Jan 2015; revised 20 Feb 2015; accepted 23 Feb 2015; published 2 Apr 2015

11. K. Wiesauer, M. Pircher, E. Götzinger, S. Bauer, R. Engelke, G. Ahrens, G. Grützner, C. K. Hitzenberger, and D. Stifter, "En-face scanning optical coherence tomography with ultra-high resolution for material investigation," Opt. Express **13**(3), 1015–1024 (2005).
12. D. M. Koller, G. Hannesschläger, M. Leitner, and J. G. Khinast, "Non-destructive analysis of tablet coatings with optical coherence tomography," Eur. J. Pharm. Sci. **44**(1-2), 142–148 (2011).
13. J. J. Liu, A. J. Witkin, M. Adhi, I. Grulkowski, M. F. Kraus, A. H. Dhalla, C. D. Lu, J. Hornegger, J. S. Duker, and J. G. Fujimoto, "Enhanced vitreous imaging in healthy eyes using swept source optical coherence tomography," PLoS ONE **9**(7), e102950 (2014).
14. J. S. Duker, P. K. Kaiser, S. Binder, M. D. de Smet, A. Gaudric, E. Reichel, S. R. Sadda, J. Sebag, R. F. Spaide, and P. Stalmans, "The International Vitreomacular Traction Study Group classification of vitreomacular adhesion, traction, and macular hole," Ophthalmology **120**(12), 2611–2619 (2013).
15. M. Kernt, I. Hadi, F. Pinter, F. Seidensticker, C. Hirneiss, C. Haritoglou, A. Kampik, M. W. Ulbig, and A. S. Neubauer, "Assessment of diabetic retinopathy using nonmydriatic ultra-widefield scanning laser ophthalmoscopy (Optomap) compared with ETDRS 7-field stereo photography," Diabetes Care **35**(12), 2459–2463 (2012).
16. R. F. Spaide, "Peripheral areas of nonperfusion in treated central retinal vein occlusion as imaged by wide-field fluorescein angiography," Retina **31**(5), 829–837 (2011).
17. L. Reznicek, T. Wasfy, C. Stumpf, A. Kampik, M. Ulbig, A. S. Neubauer, and M. Kernt, "Peripheral fundus autofluorescence is increased in age-related macular degeneration," Invest. Ophthalmol. Vis. Sci. **53**(4), 2193–2198 (2012).
18. O. Pomerantzeff, "Equator-Plus Camera," Invest. Ophthalmol. **14**(5), 401–406 (1975).
19. A. S. Neubauer, A. Yu, C. Haritoglou, and M. W. Ulbig, "Peripheral retinal changes in acute retinal necrosis imaged by ultra widefield scanning laser ophthalmoscopy," Acta Ophthalmol. Scand. **83**(6), 758–760 (2005).
20. M. Kernt, U. C. Schaller, C. Stumpf, M. W. Ulbig, A. Kampik, and A. S. Neubauer, "Choroidal pigmented lesions imaged by ultra-wide-field scanning laser ophthalmoscopy with two laser wavelengths (Optomap)," Clin. Ophthalmol. **4**, 829–836 (2010).
21. B. Povazay, B. Hermann, B. Hofer, V. Kajić, E. Simpson, T. Bridgford, and W. Drexler, "Wide-field optical coherence tomography of the choroid in vivo," Invest. Ophthalmol. Vis. Sci. **50**(4), 1856–1863 (2008).
22. B. Potsaid, B. Baumann, D. Huang, S. Barry, A. E. Cable, J. S. Schuman, J. S. Duker, and J. G. Fujimoto, "Ultrahigh speed 1050nm swept source/Fourier domain OCT retinal and anterior segment imaging at 100,000 to 400,000 axial scans per second," Opt. Express **18**(19), 20029–20048 (2010).
23. T. Klein, W. Wieser, C. M. Eigenwillig, B. R. Biedermann, and R. Huber, "Megahertz OCT for ultrawide-field retinal imaging with a 1050 nm Fourier domain mode-locked laser," Opt. Express **19**(4), 3044–3062 (2011).
24. R. J. Zawadzki, S. S. Choi, A. R. Fuller, J. W. Evans, B. Hamann, and J. S. Werner, "Cellular resolution volumetric in vivo retinal imaging with adaptive optics-optical coherence tomography," Opt. Express **17**(5), 4084–4094 (2009).
25. Y. Li, G. Gregori, B. L. Lam, and P. J. Rosenfeld, "Automatic montage of SD-OCT data sets," Opt. Express **19**(27), 26239–26248 (2011).
26. W. Choi, K. J. Mohler, B. Potsaid, C. D. Lu, J. J. Liu, V. Jayaraman, A. E. Cable, J. S. Duker, R. Huber, and J. G. Fujimoto, "Choriocapillaris and Choroidal Microvasculature Imaging with Ultrahigh Speed OCT Angiography," PLoS ONE **8**(12), e81499 (2013).
27. S. Makita, F. Jaillon, M. Yamanari, M. Miura, and Y. Yasuno, "Comprehensive in vivo micro-vascular imaging of the human eye by dual-beam-scan Doppler optical coherence angiography," Opt. Express **19**(2), 1271–1283 (2011).
28. T. Klein, W. Wieser, L. Reznicek, A. Neubauer, A. Kampik, and R. Huber, "Multi-MHz retinal OCT," Biomed. Opt. Express **4**(10), 1890–1908 (2013).
29. G. Parlitsis, M. Witmer, S. Patel, and S. Kiss, "Comparison of ultra wide-field fluorescein angiography using the Optos(R) P200Tx and Heidelberg Spectralis(R) the non-contact wide-angle lens," Invest. Ophthalmol. Vis. Sci. **54**, 16 (2013).
30. A. S. Neubauer, M. Kernt, C. Haritoglou, S. G. Priglinger, A. Kampik, and M. W. Ulbig, "Nonmydriatic screening for diabetic retinopathy by ultra-widefield scanning laser ophthalmoscopy (Optomap)," Graefes Arch. Clin. Exp. Ophthalmol. **246**(2), 229–235 (2008).
31. W. J. Donnelly 3rd and A. Roorda, "Optimal pupil size in the human eye for axial resolution," J. Opt. Soc. Am. A **20**(11), 2010–2015 (2003).
32. R. J. Zawadzki, S. M. Jones, S. S. Olivier, M. T. Zhao, B. A. Bower, J. A. Izatt, S. Choi, S. Laut, and J. S. Werner, "Adaptive-optics optical coherence tomography for high-resolution and high-speed 3D retinal in vivo imaging," Opt. Express **13**(21), 8532–8546 (2005).
33. W. Drexler and J. G. Fujimoto, *Optical coherence tomography: technology and applications* (Springer, 2008).
34. M. Hagen-Eggert, P. Koch, and G. Hüttmann, "Analysis of the signal fall-off in spectral domain optical coherence tomography systems," in *Optical Coherence Tomography and Coherence Domain Optical Methods in Biomedicine XVI*, Proceedings of SPIE 2012), 82131K.
35. R. F. Spaide, H. Koizumi, and M. C. Pozzoni, "Enhanced depth imaging spectral-domain optical coherence tomography," Am. J. Ophthalmol. **146**(4), 496–500 (2008).
36. H. Gross, W. Singer, M. Totzeck, F. Blechinger, B. Achtner, B. Dörband, and H. Müller, *Handbook of Optical Systems* (Wiley Online Library, 2005), Vol. 4.

#232125 - $15.00 USD Received 7 Jan 2015; revised 20 Feb 2015; accepted 23 Feb 2015; published 2 Apr 2015

37. S. Yun, G. Tearney, J. de Boer, and B. Bouma, "Removing the depth-degeneracy in optical frequency domain imaging with frequency shifting," Opt. Express **12**(20), 4822–4828 (2004).
38. B. R. Biedermann, W. Wieser, C. M. Eigenwillig, G. Palte, D. C. Adler, V. J. Srinivasan, J. G. Fujimoto, and R. Huber, "Real time en face Fourier-domain optical coherence tomography with direct hardware frequency demodulation," Opt. Lett. **33**(21), 2556–2558 (2008).
39. S. Makita, Y. Hong, M. Yamanari, T. Yatagai, and Y. Yasuno, "Optical coherence angiography," Opt. Express **14**(17), 7821–7840 (2006).
40. S. Martinez-Conde, S. L. Macknik, X. G. Troncoso, and D. H. Hubel, "Microsaccades: a neurophysiological analysis," Trends Neurosci. **32**(9), 463–475 (2009).
41. B. Povazay, B. Hofer, C. Torti, B. Hermann, A. R. Tumlinson, M. Esmaeelpour, C. A. Egan, A. C. Bird, and W. Drexler, "Impact of enhanced resolution, speed and penetration on three-dimensional retinal optical coherence tomography," Opt. Express **17**(5), 4134–4150 (2009).
42. T. Klein, W. Wieser, R. André, C. M. Eigenwillig, and R. Huber, "The effect of (micro-) saccades on the image quality of ultrawide-field multi-Megahertz-OCT data," in *BIOS,* (San Francisco, 2012).
43. I. Grulkowski, J. J. Liu, B. Potsaid, V. Jayaraman, C. D. Lu, J. Jiang, A. E. Cable, J. S. Duker, and J. G. Fujimoto, "Retinal, anterior segment and full eye imaging using ultrahigh speed swept source OCT with vertical-cavity surface emitting lasers," Biomed. Opt. Express **3**(11), 2733–2751 (2012).
44. B. Potsaid, V. Jayaraman, J. G. Fujimoto, J. Jiang, P. J. S. Heim, and A. E. Cable, "MEMS tunable VCSEL light source for ultrahigh speed 60kHz-1MHz axial scan rate and long range centimeter class OCT imaging," in *Optical Coherence Tomography and Coherence Domain Optical Methods in Biomedicine Xvi*, Proceedings of SPIE 2012), 82130M.
45. R. Huber, M. Wojtkowski, and J. G. Fujimoto, "Fourier Domain Mode Locking (FDML): A new laser operating regime and applications for optical coherence tomography," Opt. Express **14**(8), 3225–3237 (2006).
46. W. Wieser, B. R. Biedermann, T. Klein, C. M. Eigenwillig, and R. Huber, "Multi-megahertz OCT: High quality 3D imaging at 20 million A-scans and 4.5 GVoxels per second," Opt. Express **18**(14), 14685–14704 (2010).
47. O. P. Kocaoglu, T. L. Turner, Z. Liu, and D. T. Miller, "Adaptive optics optical coherence tomography at 1 MHz," Biomed. Opt. Express **5**(12), 4186–4200 (2014).
48. N. Suehira, S. Ooto, M. Hangai, K. Matsumoto, N. Tomatsu, T. Yuasa, K. Yamada, and N. Yoshimura, "Three-beam spectral-domain optical coherence tomography for retinal imaging," J. Biomed. Opt. **17**(10), 106001 (2012).
49. E. Beaurepaire, A. C. Boccara, M. Lebec, L. Blanchot, and H. Saint-Jalmes, "Full-field optical coherence microscopy," Opt. Lett. **23**(4), 244–246 (1998).
50. I. Zeylikovich, A. Gilerson, and R. R. Alfano, "Nonmechanical grating-generated scanning coherence microscopy," Opt. Lett. **23**(23), 1797–1799 (1998).
51. T. Bonin, G. Franke, M. Hagen-Eggert, P. Koch, and G. Hüttmann, "In vivo Fourier-domain full-field OCT of the human retina with 1.5 million A-lines/s," Opt. Lett. **35**(20), 3432–3434 (2010).
52. T. Bonin, M. Hagen-Eggert, G. Franke, P. Koch, and G. Hüttmann, "Ultra highspeed in-vivo Fourier domain full-field OCT of the human retina," in *Optical Coherence Tomography and Coherence Domain Optical Methods in Biomedicine XV*, SPIE Proceedings 2011), 788906.
53. D. J. Fechtig, T. Schmoll, B. Grajciar, W. Drexler, and R. A. Leitgeb, "Line-field parallel swept source interferometric imaging at up to 1 MHz," Opt. Lett. **39**(18), 5333–5336 (2014).
54. R. D. Ferguson, D. X. Hammer, L. A. Paunescu, S. Beaton, and J. S. Schuman, "Tracking optical coherence tomography," Opt. Lett. **29**(18), 2139–2141 (2004).
55. K. V. Vienola, B. Braaf, C. K. Sheehy, Q. Yang, P. Tiruveedhula, D. W. Arathorn, J. F. de Boer, and A. Roorda, "Real-time eye motion compensation for OCT imaging with tracking SLO," Biomed. Opt. Express **3**(11), 2950–2963 (2012).
56. G. Geregori and P. J. Rosenfeld, "Using OCT Fundus Images to Evaluate the Performance of the Spectralis OCT Eye Tracking System (Poster 1032/A434," ARVO Annual Meeting 2011.
57. R. Huber, D. C. Adler, and J. G. Fujimoto, "Buffered Fourier domain mode locking: unidirectional swept laser sources for optical coherence tomography imaging at 370,000 lines/s," Opt. Lett. **31**(20), 2975–2977 (2006).
58. C. C. Rosa and A. G. Podoleanu, "Limitation of the achievable signal-to-noise ratio in optical coherence tomography due to mismatch of the balanced receiver," Appl. Opt. **43**(25), 4802–4815 (2004).
59. B. Winn, D. Whitaker, D. B. Elliott, and N. J. Phillips, "Factors affecting light-adapted pupil size in normal human subjects," Invest. Ophthalmol. Vis. Sci. **35**(3), 1132–1137 (1994).
60. J. Polans, B. Jaeken, R. P. McNabb, P. Artal, and J. A. Izatt, "Wide-field optical model of the human eye with asymmetrically tilted and decentered lens that reproduces measured ocular aberrations," Optica **2**(2), 124–134 (2015).

1. Introduction

Optical Coherence Tomography (OCT) typically uses near-infrared light to non-invasively create volumetric images of biological samples [1]. Cross sectional examination of the human retina in ophthalmology was the first and is still the most important application of OCT [2–4], besides intravascular imaging [5], other endoscopic applications [6–8], dermatology [9],

#232125 - $15.00 USD Received 7 Jan 2015; revised 20 Feb 2015; accepted 23 Feb 2015; published 2 Apr 2015

dentistry [10] or even monitoring of industrial processes [11, 12]. Regarding ophthalmology, most commercially available and many research OCT devices provide a field of view (FOV) of about 20°x20°, measured from the nodal point of the eye (all angles in this manuscript will follow this convention; see Fig. 1). While this was sufficient to establish OCT as the most important imaging device for examining the retina [4], for many diseases a wider FOV is desirable. This includes changes of the vitreous and vitreomacular interface [13, 14], as well as retinal and choroidal diseases. For diseases such as diabetic retinopathy [15] or vascular occlusions [16], the importance of the retinal periphery is well known. Increasingly, also an interdependency to macular changes is recognized, even for diseases thought to be exclusively diseases of the fovea such as age-related macular degeneration [17]. Considering non-OCT imaging without depth information, the coverage of extremely wide viewing angles of up to 148° was possible with an experimental fundus camera using a direct contact lens [18]. However, this camera design did not find wide spread clinical application due to the low image quality, complicated measurement procedure and patient discomfort. Several years ago imaging techniques based on scanning laser ophthalmoscopy (SLO) became commercially available, enabling simple, high quality clinical widefield imaging [19]. This simplified imaging of peripheral diseases such as retinal or choroidal changes including choroidal melanoma [20]. However, widefield SLOs and fundus cameras only offer two dimensional data with no depth and no full volumetric information.

Based on the increasing interest in wider field retinal imaging, several groups have demonstrated OCT systems with increased FOV: For example 3D (three-dimensional) wide field images with ~40° FOV were shown in [21, 22] and we demonstrated ultra-widefield measurements with >60° FOV in [23]. The company Optovue recently presented their Avanti XR® OCT system allowing 40° widefield imaging and Heidelberg Engineering provided a widefield module for 55° imaging with the Spectralis® OCT system. This underlines the growing commercial interest in OCT machines with larger FOV.

Ultra-widefield OCT data can be acquired in a single step or, alternatively, by mosaicking, where several individual data sets are stitched together in post-processing. This technique is well-known in digital 2D photography, but can also be applied for 3D volumes as demonstrated in adaptive optics OCT for a small FOV with very dense sampling [24] or for standard OCT with a mosaicked FOV of 50°x35° [25]. Regarding larger imaging angles, registered OCT en face projections and angiography with FOVs of up to 107°x10° were presented in [26]. The high aspect ratio simplifies the stitching since the overlapping process only needs to fit single edges of the images, no real 2D matching is required. Widefield en face projections of OCT angiography with a lower aspect ratio and 53°x67° FOV have been presented in [27]. A major drawback of mosaicking is the increased measurement time for a whole volume which depends on the scanning angle of the OCT device and the desired FOV. This effect is especially pronounced for the most modern OCT engines with line rates in excess of several 100kHz, where the actual realignment or refixation of the patient dominates the acquisition time. Post-processing also becomes more complex as the individual volumes not only need to be translated and rotated [24] but also have to be distorted and adapted in three dimensions for a correct alignment. Typical registration errors of the stitching for wide FOVs are about ~45-60µm [25].

Here, we present isotropically, densely sampled ultra-widefield retinal OCT up to 100°. In vivo imaging data is acquired with 85° and 100° FOV in single volume acquisition and with 100° FOV using low tile number mosaicking (5 patches of 60°). This is an increase by almost a factor of three in surface area compared to our previous results with 60° FOV using our MHz-OCT [28]. To the best of our knowledge, this is currently the largest retinal volume imaged with OCT. Additionally, we will discuss challenges related to retinal ultra widefield OCT imaging and investigate how much our imaging results are affected by them.

#232125 - $15.00 USD Received 7 Jan 2015; revised 20 Feb 2015; accepted 23 Feb 2015; published 2 Apr 2015

2. Background

Higher imaging angles bring multiple challenges which need to be met. Some affect 2D as well as 3D imaging and some are specific for 3D OCT imaging only. We will outline the most important ones in this chapter. In the following chapters, our system will be characterized regarding these challenges and their influence on our imaging results will be discussed.

1.) Pupillary and ciliary shadowing is well known from many ophthalmic ultra-widefield devices [29, 30]. These artifacts can be avoided by carefully aligning the subject relative to the device [16], but it becomes increasingly more difficult with larger FOV. Other effects like involuntary eye movements further complicate the process, especially in a clinical setup where patients might have difficulties in fixating. Using a contact lens avoids ciliary shadowing, but the necessary local anesthetization increases the patient discomfort. This also applies for other potential contact solutions such as using lid specula or taping the lid and/or eye cilia.

2.) Optical aberrations generally also become more severe with a greater FOV. With sufficient effort they can be reduced for the optical system of the device, however, the ones of the human eye might be difficult to compensate as they vary from patient to patient [31]. In non-confocal 2D imaging, aberrations mainly result in a loss of transverse resolution, while in OCT and other confocal imaging techniques they additionally reduce the collection efficiency which lowers the signal to noise ratio [32].

3.) The curvature of the retina becomes an increasing challenge with a larger FOV and generates three additional problems - specifically in a clinical setup where large inter-patient differences in eye shape occur, e.g. in myopia. First, the imaging optics have to be designed to avoid that the focal region shifts away from the retina for large angles. The consequences of such a *focal shift* are the same as for optical aberrations: A decreasing transverse resolution for non-confocal 2D imaging and additionally a loss of signal for 3D OCT and other confocal imaging techniques.

The other two problems are specific to OCT. In OCT the optical path length changes over the scanning angle due to the eye's curvature. This results in artificially curved OCT images. Additionally, this curvature artifact mainly depends on the adjustment of the subject relative to the patient interface. To discuss this matter, we define the pivot point as the ideal relay image of the scanning engine, i.e. the point in which the center ray of all scanned beams crosses (see Fig. 1, Point "P"). As the distance of the pivot point relative to the front of the eye *d'* is critical in this respect, we analytically approximated its influence on the interbeam optical path length difference (iOPD) between the central ray (length *d*) and the most extreme ray (length *x*) depending on the FOV according to Fig. 1(A). Therefore we assumed that the eye is a sphere filled with water (refractive index $n = 1.33$) and with a radius of $r = 12.5$mm. Any contribution introduced by the optics of the OCT system or the eye up to the pivot point was neglected. Simulations of our 60° imaging setup [23] with ray tracing software (WinLens) showed that this neglection is justified. Therefore the iOPD can be derived as follows:

$$iOPD = n \cdot [d - x] = n \cdot [(2 - \cos\varepsilon)r - (1 - \cos\varepsilon)d' - \sqrt{r^2 - (r - d')^2 \sin^2\varepsilon}] \quad (1.1)$$

A plot of this equation as a function of the FOV (2ε) with the parameter d' is displayed in Fig. 1(B). The iOPD issue does not only make reconstruction of the real eye shape difficult, but also has two consequences which make imaging more challenging: On the one hand, the *sensitivity roll off* [33, 34] decreases the signal towards one end of the axial imaging range. This reduces the perceived image quality either in the center or towards the periphery, depending on whether enhanced depth imaging [35] is used or not, respectively. The magnitude of this effect depends on the resolution of the spectrometer in spectral domain OCT (SD-OCT) and on the instantaneous line width of the swept laser source in swept source OCT (SS-OCT). In general, SS-OCT systems provide a better sensitivity roll-off performance

#232125 - $15.00 USD Received 7 Jan 2015; revised 20 Feb 2015; accepted 23 Feb 2015; published 2 Apr 2015

compared to SD-OCT, suggesting that SS-OCT will be the technology of choice for ultra-widefield OCT in the future.

On the other hand, the iOPD difference might lead to a *cropped image* because the retina will move out of the axial imaging range toward the edges. This is especially a problem for SD-OCT systems which generally have a lower imaging range compared to SS-OCT. For example, at a FOV of 100° and a pivot point positioned near the nodal point of the eye (d' = 7.5mm) [36], the iOPD equals 2.8mm according to Eq. (1).1. If we assume a thickness of the relevant structures, i.e. retina and choroid, of 1mm (measured in air), the system needs a minimum imaging range of 3.8mm. This value does not even include any overhead accounting for patient movement and misalignment. 3.8mm is more than the typical range of SD-OCT. So most likely, future commercial >80° FOV OCT systems will be SS-OCT. Theoretically the two effects related to iOPD can be compensated by either using a reference arm whose length is adjusted rapidly or with a special optical design of the sample arm. Also systems which use an optical or electronic frequency shifter [37, 38] could use frequency tracking to compensate this effect.

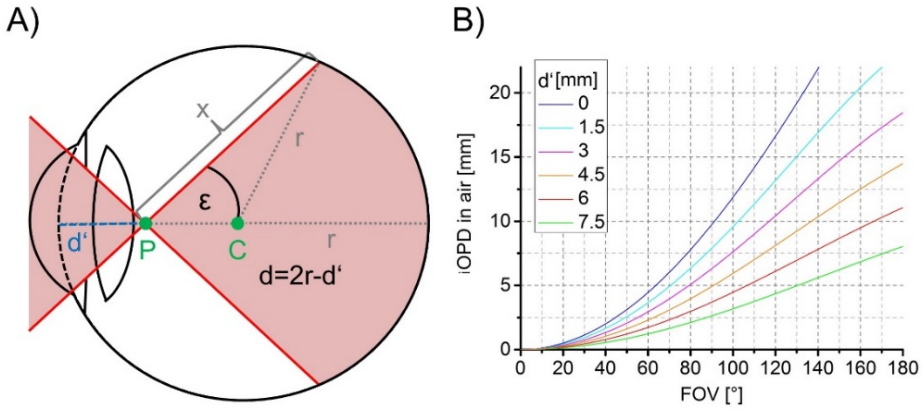

Fig. 1. A) Schematic illustrating artificially introduced interbeam optical path length differences (iOPD) in retinal OCT imaging between the central ray with the length $d = 2r\text{-}d'$ and the most extreme ray with the length x. P is the pivot point of the scanning optics, C the center of the eye, p the distance between P and the front of the sphere and r the radius of the eye. The scanned beam is illustrated in red. 2ε correspond to the FOV. B) iOPD between d and x plotted as a function of the FOV for various values of the parameter d'.

4.) The high number of A-scans per volume is also a challenge in ultra-widefield OCT imaging. For high quality images with good visibility of small details, the system should not only have a high transverse optical resolution but it should also have a sufficiently dense sample spacing, at least matching the resolution value, but ideally 2-4 times more. Therefore the number of A-scans per volume increases quadratically with the FOV. E.g. a scan over 85°x85° or 25.5x25.5mm^2 with a spot size of 20µm should have at least 1275x1275 A-scans ≈1.6 Mio A-scans to achieve dense sampling with one measurement per spot size. If one would also like to perform OCT angiography [39] over such wide FOVs, where the same location needs to be rescanned multiple times, an even higher number of A-scans would be required. Capturing such a high number of A-scans without motion artifacts requires a system with a high line rate. Changes in retinal position are typically a result of slow continuous drifts or rapid microsaccades, which occur according to literature every ~0.5-2s during a prolonged fixation [40]. If multiple successive volumes are acquired, an acquisition time of 1-2s is sufficient for an artifact free data set for most subjects [41, 42]. Therefore A-scan rates on the order of ~1MHz are required for standard OCT measurements. Few OCT systems

#232125 - $15.00 USD Received 7 Jan 2015; revised 20 Feb 2015; accepted 23 Feb 2015; published 2 Apr 2015

fulfill this demand while maintaining a suitable sensitivity close to 90dB or higher [28]: Retinal imaging data with a SS-OCT system based on a 1060nm VCSEL with up to 580kHz line rate has been presented in [43]. At 1310nm, which is unsuitable for imaging the posterior eye, even 1MHz is feasible with VCSEL technology [44]. We have shown Fourier domain mode locked (FDML) lasers [45] with A-Scan rates of up to 3.35MHz at 1060nm [28] or 5.2MHz at 1310nm [46]. If the imaging speed of a system does not suffice, acquisition can be parallelized. In SD-OCT, O. Kocaoglu et al. presented the use of four synchronized spectrometers with a total line rate of 1MHz [47]. Another idea is to use multiple spots on the sample [48]. In the case of retinal SS-OCT 6.7MHz [28] were presented and at 1310nm even 20.8MHz [46]. More sophisticated techniques for parallelization are full field OCT (FF-OCT) [49] and line field OCT (LF-OCT) [50]. For FF-OCT of the human eye 6.8 million A-scans/s have been demonstrated [51, 52], although FF-OCT intrinsically suffers from the lack of confocal gating resulting in a reduced image quality due to cross talk. LF-OCT offers confocal gating in one dimension reducing the cross talk. Here imaging with an effective line rate of up to 1MHz has been shown [53]. As an alternative, the lack of fast imaging speed can be compensated to a certain limit by employing an eye tracker [54], which increases the system complexity and cost: The hardware of the system has to be extended by an additional imaging method fast enough to resolve eye motion during the frames. This is typically either an integrated SLO system with secondary beam steering mechanism or an infrared fundus camera [55]. In addition, software algorithms are required to compensate the eye motion with the scanning mirrors of OCT system or re-scan corrupted B-frames. Tracking bandwidths around 1kHz [54, 55] and motion reduction down to 1.6µm [55] have been reported for research systems. Accuracies reported for commercial devices are lower [56]. However even research grade systems still have limitations like a latency between the eye motion and correction of it, which are discussed in [55] in more detail. Even though possible, it would also be extremely inconvenient for a patient having an OCT examination with a duration of several minutes of continuous target fixation. So for ultra-widefield OCT with >90° FOV, scan rates of at least several hundred kHz, ideally above 1 MHz are required for practical use in the clinic.

5.) The performance of the fast axis galvo scanner can become a limiting factor in retinal ultra-widefield OCT imaging as well – especially when imaging at high speeds. The scanning frequency of the fast axis galvo scanner equals the ratio of the line rate over the desired number of A-scans. For MHz-OCT, typical scanning frequencies are around 500Hz at unidirectional scanning. In order to achieve sufficiently high FOVs at such high rates, the telescope located after the scanning mirrors can be used as optical leverage to increase the scan angle on the eye. However this technique reduces the beam diameter on the pupil.

3. Experiments

This chapter will first give a short outline on the general layout of our system including the FDML swept laser source, interferometer design and electronics involving the data acquisition. Then, the main focus will lie on the design considerations and performance characterization of the free space optics in the sample arm which are specifically tailored to the wide FOV.

3.1 General system layout

The SS-OCT system is based on a 1060nm FDML laser similar to the one demonstrated and characterized in [28] but without an intracavity Ytterbium (Yb) amplifier. It was operated with a 4x buffering stage [57] quadrupling the fundamental FDML frequency of 420kHz to an effective line rate of 1.68MHz, which is sufficient for the *high number of A-scans per volume* as discussed in chapter 2. Despite the missing Yb amplifier, a 70nm sweep range was possible resulting in a measured axial resolution of 14µm in air.

#232125 - $15.00 USD Received 7 Jan 2015; revised 20 Feb 2015; accepted 23 Feb 2015; published 2 Apr 2015

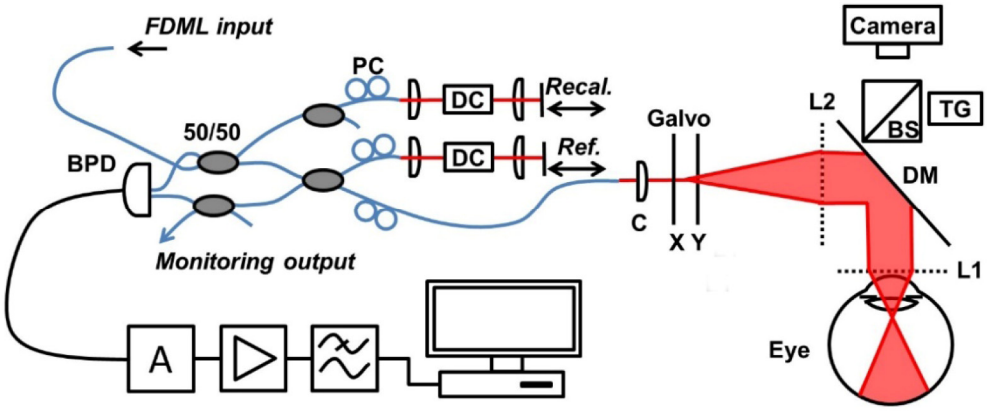

Fig. 2. Interferometer and sample arm layout. Black connections are electrical wires, blue connections are Hi1060 fibers and free space beams are red. BPD: Balanced photo detector, 50/50: fiber coupler with symmetric splitting ratio, PC: polarization controller, DC: dispersion compensation, C: collimator lens with 18.4mm focal length, L1: ophthalmic lens (either four spherical lenses with 300mm focal length each, Volk 78D or Volk SPXL), L2: four spherical lenses with either 300 mm or 200mm focal length each, DM: dichroic mirror with >99.9% reflectivity for 1000nm-1090nm wavelength, BS: 50/50 beam splitter for 400nm-700nm, TG: fixation target (video projector with OD3 neutral density filter), the signal from the BPD is attenuated, then amplified and low pass filtered before acquisition

We used a fiber based Michelson-like interferometer design (see Fig. 2) as introduced in [23]. It features two spectrally equalized and flattened output ports for a dual balanced photo detector. This is necessary to achieve shot-noise limited detection, if the laser source has a significant noise level [58]. Additionally, the interferometer has a recalibration arm for k-space resampling. It is sufficient to acquire one recalibration curve before each acquisition, as the sweep to sweep variation of the time wavelength evolution is very small in an FDML laser. Therefore no k-clock is required in our setup.

A 1GHz dual balanced photo diode (WL-BPD1GA, Wieserlabs) was used for OCT signal detection. The electronic signal was attenuated by −5dB (VAT-5 + , Minicircuits) in order to get appropriate signal amplitude after amplification (ZFL-1000LN + , Minicircuits) for digitization with our 8bit PCIe data acquisition card (Signatec PX1500) at 1.5GS/s. A 750MHz low pass filter (BLP-750 + , Minicircuits) is inserted to avoid aliasing. This gives an imaging range of 3.4mm in air. The acquisition system was operated in streaming mode, directly transferring the data to the 24GB RAM memory of the host computer.

3.2 Sample arm design considerations

Throughout this paper, three different configurations of the sample arm are employed (see Table 1). The 60° imaging optics have already been used in previous publications [23, 28]. The 85° and the 100° imaging configuration are new, although they are based on our established design.

#232125 - $15.00 USD Received 7 Jan 2015; revised 20 Feb 2015; accepted 23 Feb 2015; published 2 Apr 2015

Table 1. Imaging setups

Name of configuration	**60° imaging setup**	**85° imaging setup**	**100° imaging setup**
Collimator	11mm aspherical (Thorlabs C220TMD-C)	18.4mm aspherical (Thorlabs A280TM-C)	
Lens L1	4x150mm≈37.5mm spherical (Thorlabs LA1417-C)	~15mm aspherical (Volk 78D)	~7.5mm aspherical (Volk Super Pupil XL)
Lens L2	4x300mm≈75mm (Thorlabs LA1256-C)		4x200mm≈37.5mm (Thorlabs LA1541-B)
Spot diam. on cornea[1]	0.64mm	0.45mm	0.33mm
Spot diam. on retina[1,2]	12.5µm	17.8µm	24.2µm
Galvo Scanners	Non-resonant (Cambridge Technology, 6215H)		
Fixation Target	LED Projector (Acer, C20), 1000x attenuated		
A-scan rate	1.68 MHz		0.84 MHz
Imaging range (in air)	3.4mm		6.8mm
Data set size (A-scans)	2088x2088		2330x2330

[1] (FWHM)
[2] estimated from eye model [36]

As displayed in Fig. 3(A), the original system consists of an 11mm collimator (Thorlabs C220TMD-C) and a telescope with two groups of four standard spherical lenses with 2" diameter. Each lens of L1 {L2} has a focal length of 150mm (Thorlabs LA1417-C) {300mm (Thorlabs LA1256-C)} resulting in an effective focal length of ~37.5mm {~75mm}. Combining multiple lenses with a lower optical power to a group with the desired focal length has the advantage of less optical aberrations in the system. However, this also increases the number of refractive surfaces in the system, which leads to slightly higher reflective losses. As we do use proper anti reflection (AR)-coating these losses should be negligible. This setup was now adapted for higher FOVs by changing the lenses L1, L2 and C as shown in Fig. 3(B) and 3(C). In the following we will explain our choices for these and other optical elements of our sample arm.

The ophthalmic lens L1 either needs to be a larger lens with a moderate optical power or a smaller lens with a higher optical power. We decided to use two rather small lenses with high optical power – a Volk 78D for 85° imaging and a Volk Super Pupil XL (SPXL) for 100° imaging. These are aspheric lenses designed for use with ophthalmic slit lamps. The lenses have a focal length of ~15mm and ~7.5mm and a diameter of 30.9mm and 19mm, respectively. Both had a custom AR-coating for 850-1100nm. An AR-coating was essential as reflectivities of up to ~60% were measured for both uncoated lenses at extreme scanning angles as displayed in Fig. 4. With an uncoated lens, we observed at larger angles that a part of the reflected light was split into a second beam, which exited L1 under a different angle. We assume that it originated from multiple internal reflections within the lens. The AR-coating improved the transmission of the lenses significantly although losses still occur and the second beam could still be observed. If we would modulate the laser output power synchronous to the galvo scan angle, we would be able to maintain constant output power levels on the cornea and compensate for these losses. For safety reasons we did not implement

#232125 - $15.00 USD Received 7 Jan 2015; revised 20 Feb 2015; accepted 23 Feb 2015; published 2 Apr 2015

such a concept. It should be noted, that besides the power on the cornea, also the collection efficiency of the backscattered light is decreased by this effect. For OCT imaging, this should not cause a visible decrease in the center at low imaging angles, but could have an effect for larger angles.

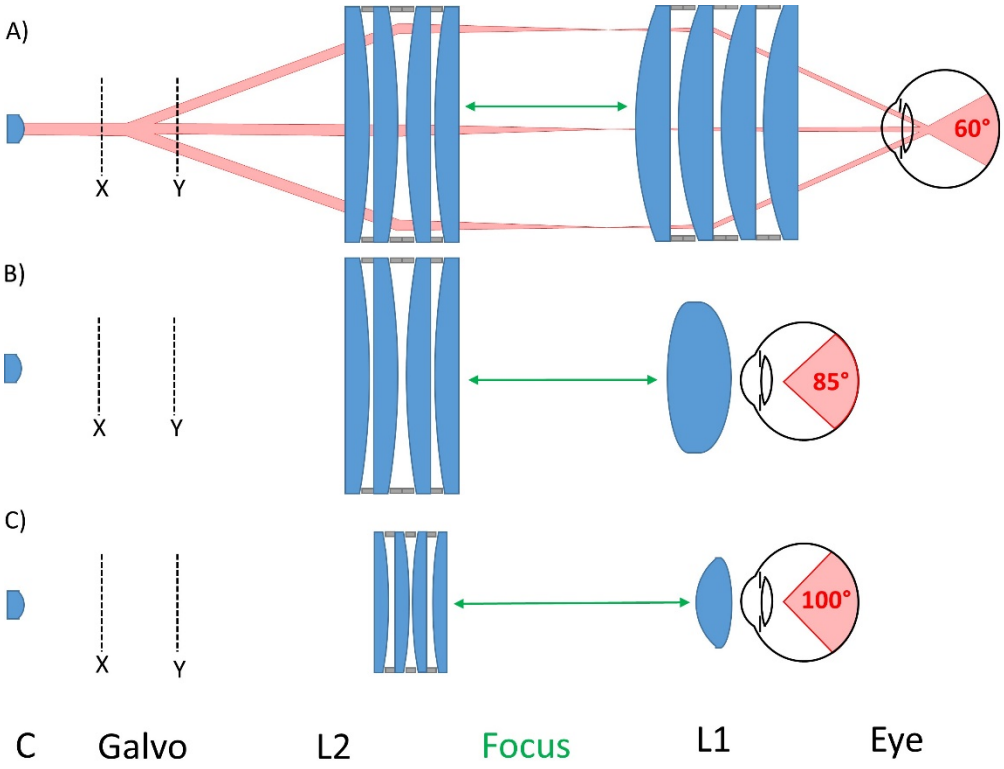

Fig. 3. Lens configurations for A) 60°, B) 85° and C) 100° imaging. Table 1 gives details on the respective lenses. Grey boxes represent retaining rings, which are 2.5mm (A and B) and 2mm thick (C). The collimated beam is deflected by two galvo mirrors, which are mounted with rotation axes ~12mm apart. Distance of L1 and L2 is varied for focusing. Exemplary beam path for central and the two most extreme galvo positions is shown in A).

The choice of the focal length of L2 is a trade-off between beam diameter after L1 and required scanning angle of the galvo mirrors. This is because the ratio of the focal lengths of L1 (f_{L1}) and L2 (f_{L2}) is proportional to the magnification of the beam diameter and inversely proportional to the multiplication factor for the scanning angle caused by this telescope. If f_{L2} is increased too much, the beam diameter decreases to a level where the spot size on the retina is too large and not enough backscattered light is collected. If it becomes too small – the required scanning angle is too large for the galvo scanners. Also, the mechanical construction gets more challenging for shorter focal lengths, as the distance between the two lenses has to be the sum of their focal lengths and spacing becomes very narrow due to the 90° reflection at the dichroic mirror, which is used for coupling in a fixation target and a pupil camera (see below). We found that a group of four standard spherical lenses with 300mm {200mm} focal length each and a combined focal length of ~75mm{~50mm} was a good compromise in combination with the Volk 78D {Volk SPXL}. The lenses have a diameter of 2" {30mm (Thorlabs LA1541-B)}.

#232125 - $15.00 USD Received 7 Jan 2015; revised 20 Feb 2015; accepted 23 Feb 2015; published 2 Apr 2015

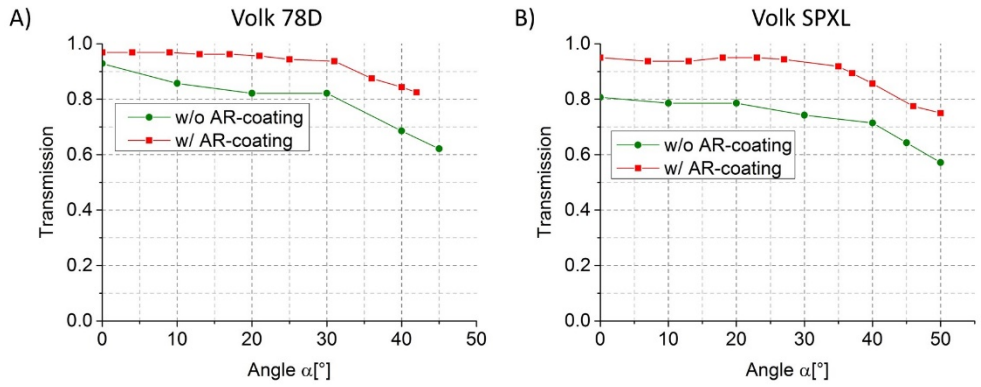

Fig. 4. Transmission of A) Volk 78D and B) Volk SPXL without and with AR-coating as a function of the angle α (measured from the optical axis). Solid line drawn between data points.

In order to achieve an acceptable spot size on the retina a long focal length of 18.4mm was chosen for the collimator C (Thorlabs A280TM-C). With the Volk 78D we measured a beam diameter of 0.45mm (FWHM) and 0.33mm for the Volk SPXL on the cornea. This results in a theoretical spot size of 17.4µm or 23.8µm, respectively, on the retina.

Other components of the sample arm in our original as well as in the new design include a dichroic mirror which has >99.9% reflectivity from 1000nm to 1090nm with a diameter of 3" for the original 60° design and the Volk 78D and 1" for the Volk SPXL. The camera behind the mirror is a standard webcam (Logitech), which is used for initial coarse alignment. The fixation target is a compact LED video projector that is attenuated with a neutral density filter by a factor of 1000. This is very helpful for mosaicking as the projected target can be moved in the subject's FOV. The beam is steered with two non-resonant galvanometric scanners (Cambridge Technology, 6215H) in x- and y-direction. Their rotation axes are 12mm apart.

3.3 Characterization of sample arm performance

Regarding the critical challenges discussed in the previous chapter, we analyzed the three most relevant performance aspects of our sample arm for the three lens configurations: The stability of the pivot point to estimate the amount of possible *pupillary shadowing*, the angle dependency of the backcoupling efficiency to determine the *optical aberrations* still present in our system, and the *performance of the galvo scanner* to check whether it suffices for our system.

The stability of the pivot point over the scan angles was measured by inserting a CMOS camera into the pivot point and addressing multiple angles with the galvo mirrors. The 6.4x4.6mm^2 large camera chip was always perpendicular to the optical axis of L1. The pivot point distance to the lens was determined by minimizing the spot movement on the chip for a continuously scanning x- and y-galvo mirror.

The results for all three imaging configurations are presented in Fig. 5. The center of the beam moved in x- and y-direction by 1.72mm, 2.06mm and 1.86mm for the 60°, 85° and 100° configuration, respectively. Pupil diameters for a darkened environment vary between 4mm and 9mm - decreasing with the age of the patient [59]. While there should be no problem to aim through the pupil and even position the pivot point more closely towards the posterior eye to reduce the iOPD (see Fig. 1) for younger patients, this could become more challenging for older subjects. Pharmaceutical dilation of the pupil could simplify the alignment procedure especially if the environment cannot be darkened completely.

#232125 - $15.00 USD Received 7 Jan 2015; revised 20 Feb 2015; accepted 23 Feb 2015; published 2 Apr 2015

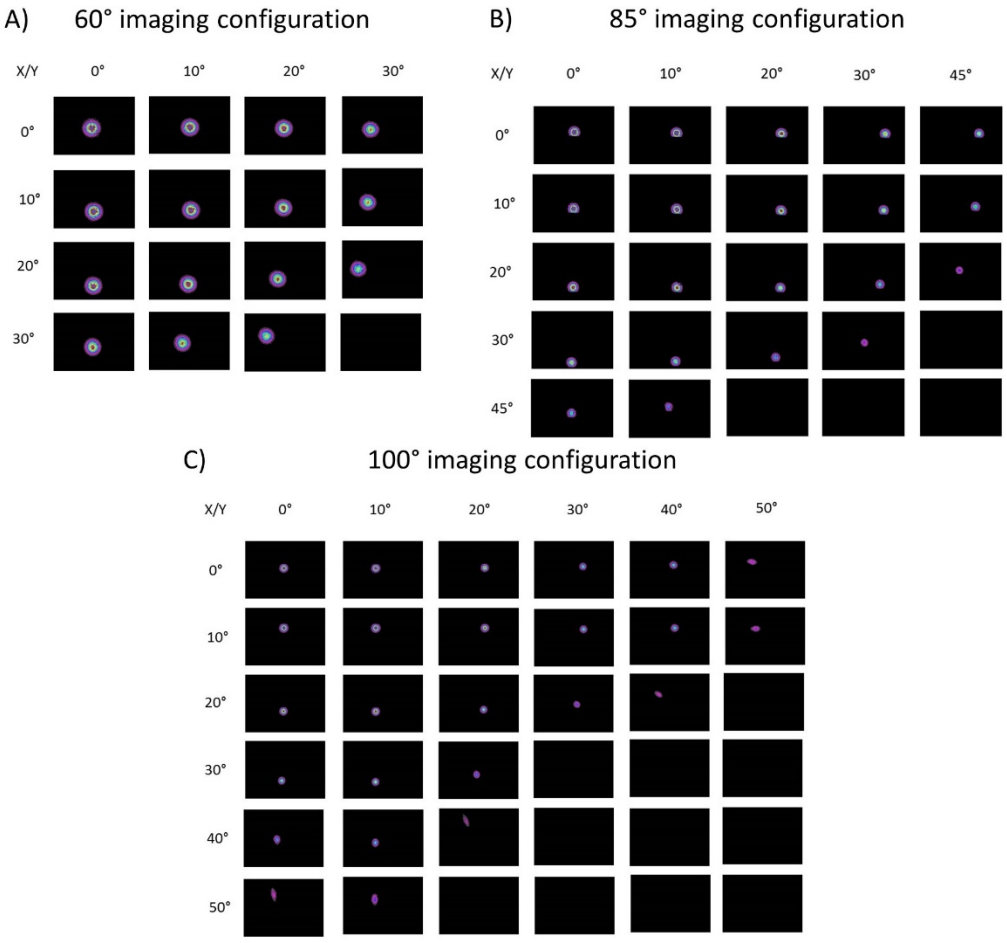

Fig. 5. Spot pattern in the pivot point for multiple galvo positions for A) 60°, B) 85° and C) 100° imaging configuration.

Furthermore we assume that an additional telescope between the two galvo mirrors should reduce the maximum deviation of the beam center. We observed that in case of one single galvo scan axis placed directly in the back focal plane of L2, scanning this only generated a negligible movement of the laser beam in the pivot point. With a double telescope both mirror axis can be exactly relay imaged into the pivot point behind L1 if each galvo is placed in the rear focal point of one telescope. In case of a single telescope, the rear focal point of the telescope is positioned in the center between the two rotation axes of the galvo mirrors. Therefore they are not exactly relay imaged into the pivot point behind L1.

The angle dependent backcoupling efficiency was measured to characterize the *optical aberrations* of our optical system. An AR-coated spherical lens with 60mm focal length (LE) and a silver mirror were mounted on a rotation and translation stage in front of L1 (see Fig. 6(A)). The beam was steered to multiple discrete angles and the optical axis of LE and the mirror was aligned to match the beam. The mirror was tilted until maximum optical power was measured at the monitoring output of our interferometer with blocked reference and recalibration arm. This value was multiplied by four (to account for the inherent loss caused by the interferometer design) and divided by the optical power measured directly after L1 for $\alpha = 0°$ to obtain the backcoupling efficiency at all angles. Hence this measurement includes the effect of the angle dependent reflectivity of the lenses (see Fig. 4). The measurement was

#232125 - $15.00 USD Received 7 Jan 2015; revised 20 Feb 2015; accepted 23 Feb 2015; published 2 Apr 2015

performed once with fixed focus (distance between L1 and L2), where it was optimized only for α = 0°, and once with focus optimization at every angle. This should give an estimation on how large a focal shift out of the imaging plane can be expected. We characterized our standard 60° imaging configuration as well our two new ultra-widefield imaging setups.

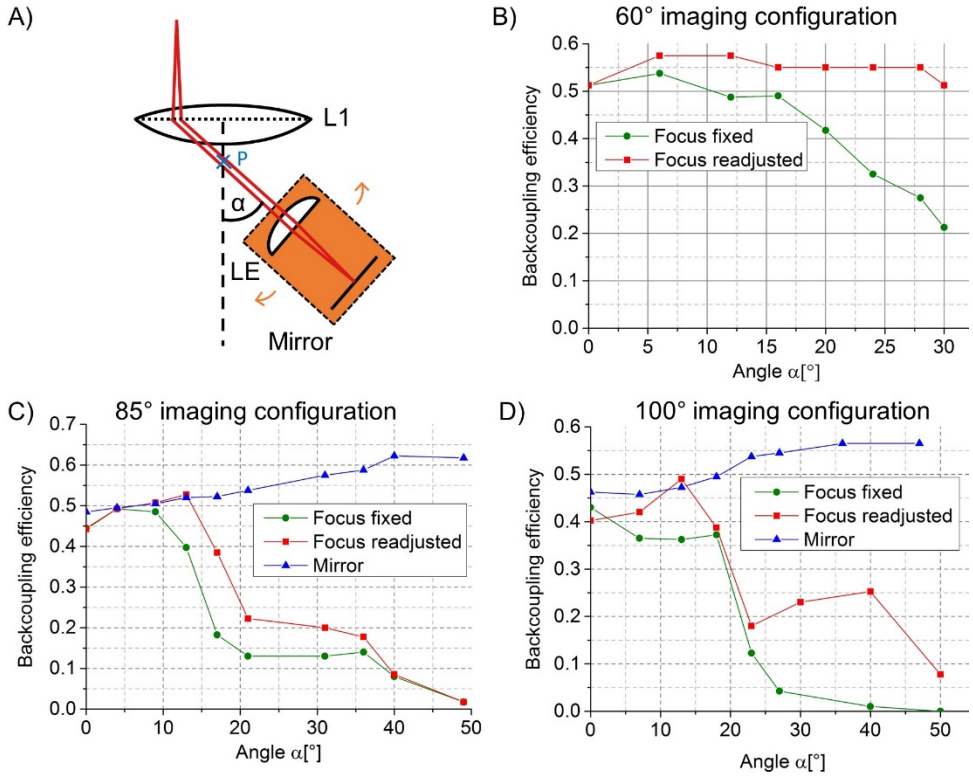

Fig. 6. Measurement of the angle dependent backcoupling efficiency. A) Schematic of the measurement procedure: A mirror mounted to a lens was rotated around the pivot point P. Backcoupling efficiency vs. angle α for the B) 60° imaging configuration C) 85° imaging configuration and D) 100° imaging configuration. Solid line drawn between datapoints.

The results for the standard 60° imaging configuration is presented in Fig. 6(B). For a fixed focus, the backcoupling efficiency remains around 50% until α = 17° and then drops almost linearly down to 21% at maximum angle. If the focus is readjusted, it remains well above 50% at all imaging angles. Necessary corrections of the focus are on order of a few mm (distance L1 and L2) compared to the fixed focus case. As there is no visible signal decrease in our 60° ultra widefield OCT images towards the edges, the focal plane should coincide well with the retina.

The performance of the 85° imaging configuration with the Volk 78D lens is displayed in Fig. 6(C). The backcoupling efficiencies in the center are only slightly below the ones of the lenses for 60° imaging. However there is a significant drop of backcoupling efficiency at α≈15° down to ~15% for a fixed focus. If focus readjustments on the order of ~1mm are made, this decrease is reduced and sets on slightly later. In order to determine whether these characteristics are related to the rest of the optical system or solely the ophthalmic lens, we replaced L1 with a plain mirror and measured backcoupling efficiency again. As it stayed above 48% independent of the galvo angle, we assume that the decrease of backcoupling efficiency is a feature of the Volk 78D's lens design.

#232125 - $15.00 USD Received 7 Jan 2015; revised 20 Feb 2015; accepted 23 Feb 2015; published 2 Apr 2015

The 100° imaging setup with the Volk SPXL lens shows similar behavior regarding the backcoupling efficiency. It remains around 40% for α<20° and decreases for larger angles. Refocusing has a greater effect in this case. The magnitude of refocusing is on the order ~1mm for this lens configuration. Interestingly the decrease towards larger angles is not monotonic - there is a second maximum at α≈40°. A measurement with the mirror replacing the Volk SPXL indicates that the decrease towards larger imaging angles is also caused by the SPXL lens. It could be possible, that this is intentional to compensate optical aberrations in the human eye or that the lens design is not optimal for our OCT system. Further investigations with optical design software would be necessary to understand this behavior. However, we can conclude at this point, that the optical performance of our assemblies consisting of 4 lenses each is almost perfect and does not generate any noticeable beam distortion - however some degree of focal shift.

For characterization of the *galvo performance*, we measured the maximum optical angle at a given frequency of the Cambridge Technologies 6215H x-galvo. The driving signal was either triangular with 70% duty cycle or sinusoidal. It had 20V peak to peak voltage, which corresponds to the specified maximum voltage. A collimated red laser beam was reflected by the scanning mirror onto a scale, which provided a resolution of 0.6°. The galvo was operated for about 10s to read the measurement value, then a pause was made until the scanner was cooled down again.

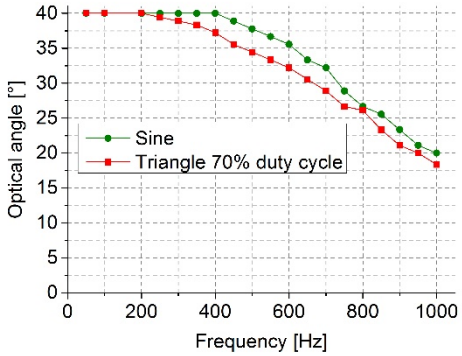

Fig. 7. Maximum optical angle vs. frequency for the Cambridge Technologies 6215H x-galvo with sinusoidal and triangular driving signal. Solid line drawn between datapoints.

The results are presented in Fig. 7. The galvo scanner can keep the specified maximum angle of 40° for a frequency of up to 400Hz and 200Hz for the sinusoidal and triangular signal, respectively. Above, the optical angle drops almost linearly with the frequency. The required optical angle of the galvo for obtaining a certain FOV depends on the lens configuration. The configurations for 60°, 85° and 100° imaging have an optical lever (ratio of f_{L2} and f_{L1}) of 2, 5 and 6.7, which requires an optical scan angle of the galvo of 30°, 17° and 15°, respectively. The required frequency depends on the A-scan rate, desired number of A-scans per B-frame and whether unidirectional with a certain duty cycle or bidirectional scanning is performed. For 60° and 85° imaging, we use 2088 A-scans per B-frame and 2300 for 100° imaging. At a line rate of 1.68 MHz and at unidirectional operation with 70% duty cycle, this results in a frequency of 563Hz and 511Hz. According to the data presented in Fig. 7, the galvo performance is sufficient for our imaging configurations. However, depending on the frequency and the amplitude of the scanner, it generates a significant amount of heat.

4. Ultra-widefield MHz-Imaging

All in vivo retinal imaging experiments were performed in accordance to the tenets of the Declaration of Helsinki. We had two male, healthy volunteers aged 26 and 31, the same eye

#232125 - $15.00 USD Received 7 Jan 2015; revised 20 Feb 2015; accepted 23 Feb 2015; published 2 Apr 2015

of each individual was imaged throughout the experiments. First we will demonstrate mydriatic and non-mydriatic OCT imaging with up to 85° FOV acquired with the Volk 78D. Then OCT data with up to 100° FOV is presented which was recorded with the Volk SPXL. This will be compared with stitching of 60° images taken with the Volk 78D, adding up to a 100° image consisting of 5 tiles.

4.1 85° imaging

For 85° imaging the sample arm was equipped a Volk 78D as the ophthalmic lens. As for all following experiments 1.6mW of optical power are incident on subject's cornea. Higher optical powers might be possible for a raster scanning device according to IEC 60825-1 if appropriate safety precautions to ensure scanning like a fast beam shutter are implemented. The measured sensitivity of 90dB is shot-noise limited if backcoupling efficiency and 3dB loss due to our interferometer design are taken into account. Scanning was unidirectional with 70% duty cycle. The acquisition of 2088x2088 A-scans took a total of 3.6s imaging time including flyback of the galvo.

First, we imaged with non-dilated pupils in a darkened room. During alignment the fast x-galvo was scanned permanently, the y-galvo was kept at central position. About ten B-frames/s were computed in real time as a preview. An en face projection of the OCT data is presented in Fig. 8(A). A corresponding B-frame extracted near the fovea is shown in subfigure C and a flythrough of all B-frames is shown in Media 1. The horizontal white line results from not perfect subtraction of the laser background. The adjustment of the distance between L1 and cornea or the pivot point and the nodal point proved to be critical due to the large image curvature. There is a trade-off between two of the challenges discussed in chapter 2: If the pivot point is placed in the center of the pupil, the image curvature is larger than if the pivot point is positioned more towards the posterior eye (see Fig. 1). If the curvature becomes too large, the imaging range and sensitivity roll-off become limiting. On the other hand pupillary shadowing is reduced if the pivot point is positioned more towards the anterior eye. We maximized the FOV by adjusting this distance and found that we could reach 80° but were limited by the 3.4mm imaging range of our system as visible in the B-frame.

In order to relax this trade-off, a pupil of volunteer one was medically dilated with tropicamide and imaging was repeated. The en face projection of the OCT data is given in Fig. 8(B). A corresponding B-frame covering the fovea region is presented in subfigure D (six times moving frame average) and E (no averaging). A flythrough of all B-frames can be found in Media 2. We would like to remark, that moving frame averaging does not cost effective imaging speed, but transverse resolution. In the case of our measurements with oversampling, the loss of transverse resolution should not be equal to the number averaged frames. This time, the pivot point could be positioned closer towards the nodal point of the eye, which decreased the image curvature significantly. The cornea was almost touched by L1. The entire B-frame width is now occupied by the retina and clipping occurred at the mounting of L1. Therefore, the maximum possible FOV of 85° was limited by the optical design of the Volk 78D.

A decrease of the signal towards the edges is visible especially in the B-frames and in the magnified views in Fig. 8(F) and 8(G). There are three possible explanations. It could be related to the two technical challenges discussed in chapter 2 or possibly a more fundamental problem: The first possible reason is, that the signal loss is caused by the curvature of the posterior eye which shifts the retina out of focus towards the edges of the image, i.e. at large angles. In this case it should be possible to increase the signal strength from the center to the edges by adjusting the focus of our optics (distance L1 and L2). Because it was not possible to achieve a visible change in signal distribution we conclude that this focusing effect is negligible. The second explanation are optical aberrations in the system and the eye, leading to reduced backcoupling efficiency towards the edges of the scan. Our measurement of the angle dependent backcoupling efficiency allows us to quantify this effect to a ~4dB signal

#232125 - $15.00 USD Received 7 Jan 2015; revised 20 Feb 2015; accepted 23 Feb 2015; published 2 Apr 2015

drop over ± 37.5° and a ~8dB signal drop over ± 42.5° (Fig. 6). The rapid signal decrease at α≈15° in the graph of Fig. 6 roughly corresponds to the size of the brighter center observed in the imaging data. So this problem is important in our current system, it can be expected that an improved lens design will eliminate it.

A third, more fundamental contribution to the signal loss over angle might be angle dependent backscattering of light in tissue. If the backscattering would have some directed, specular angle distribution, imaging the retina in the center, where the beam is perpendicular to the retina would yield more signal than imaging at the edges, where the beam is incident under a 18° angle. It should be noted that this would not be the classical angle dependent scattering distribution, because laser light and detection always stay parallel. It would be more something like a quasi-specular reflexion contribution. However, our imaging results with ± 20° offset (see next section) also have their brightest part in the center, and not at an offset of 20°, indicating that this effect, in case it exists here, is also negligible.

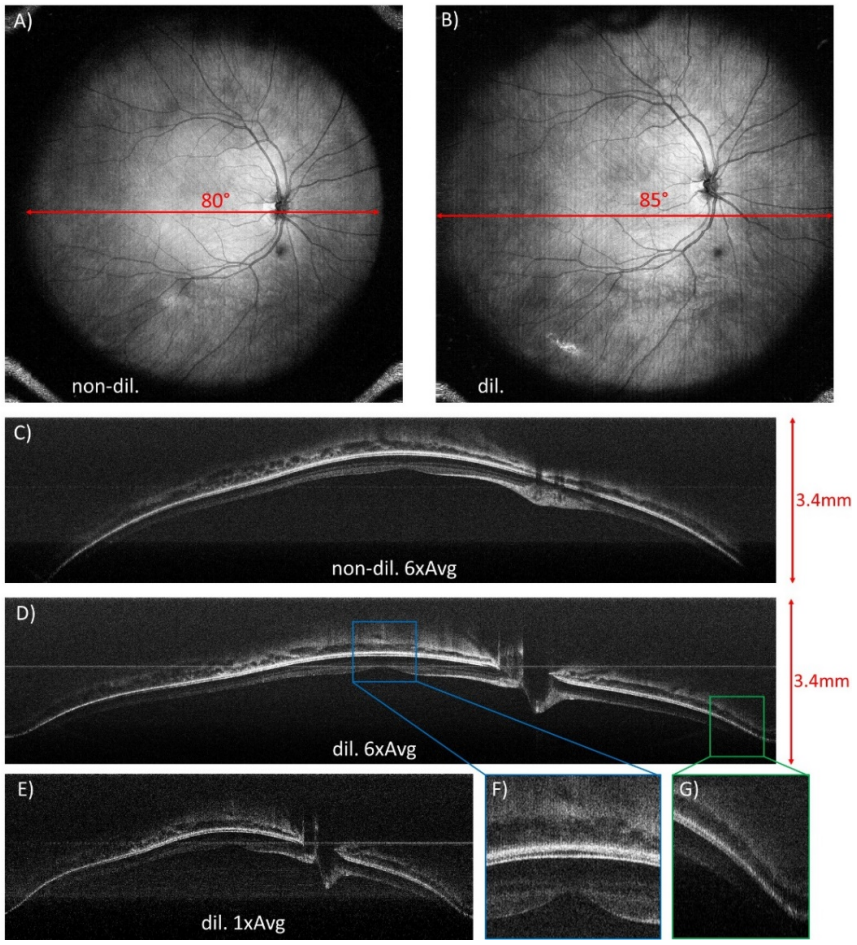

Fig. 8. Data from 85° ultra-widefield retinal in vivo OCT imaging. En face projections from imaging with a non-dilated and dilated pupil are displayed in subfigure A and B, respectively. A selected corresponding B-frame with six times moving frame averaging is given in subfigure C and D. A flythrough of all six times averaged B-frames is supplied in these two movies with 60 frames/s playback: Non-dilated (Media 1) and dilated case (Media 2). Subfigure E shows a B-frame without averaging from the dilated case. Subfigures F and G display magnifications of subfigure D at the indicated locations to visualize the angle dependent sensitivity decrease.

#232125 - $15.00 USD Received 7 Jan 2015; revised 20 Feb 2015; accepted 23 Feb 2015; published 2 Apr 2015

4.2 100° single volume imaging

For 100° single volume imaging the ophthalmic lens was switched to the Volk SPXL. In first trials we observed that the image curvature again became a limiting factor for the maximum FOV. This could not be compensated by adjustment of the pivot point position, which was only approximately 7mm from the surface of L1 away. Therefore it could be placed only very close to subject's pupil, as touching of the lens and cornea had to be avoided. Consequently we had to increase our imaging range. This would be possible by using photodiodes and a data acquisition card with significantly higher detection bandwidth and sampling rate, but neither was available during our measurements. Hence we decided to reduce the imaging speed of our MHz-OCT from 1.68MHz down to 840kHz by reducing the buffering factor of the FDML laser from 4x to 2x. The number of A-scans was increased to 2330x2330 to provide dense sampling of the increased FOV. Thus the total acquisition time for one data set increased to 8.1s. This is clearly too slow for any clinical application and even in a lab environment with healthy subjects motion artifacts are expected, but results should give an idea which other challenges need to be met for 100° ultra-widefield imaging. The sensitivity was measured to be 91dB.

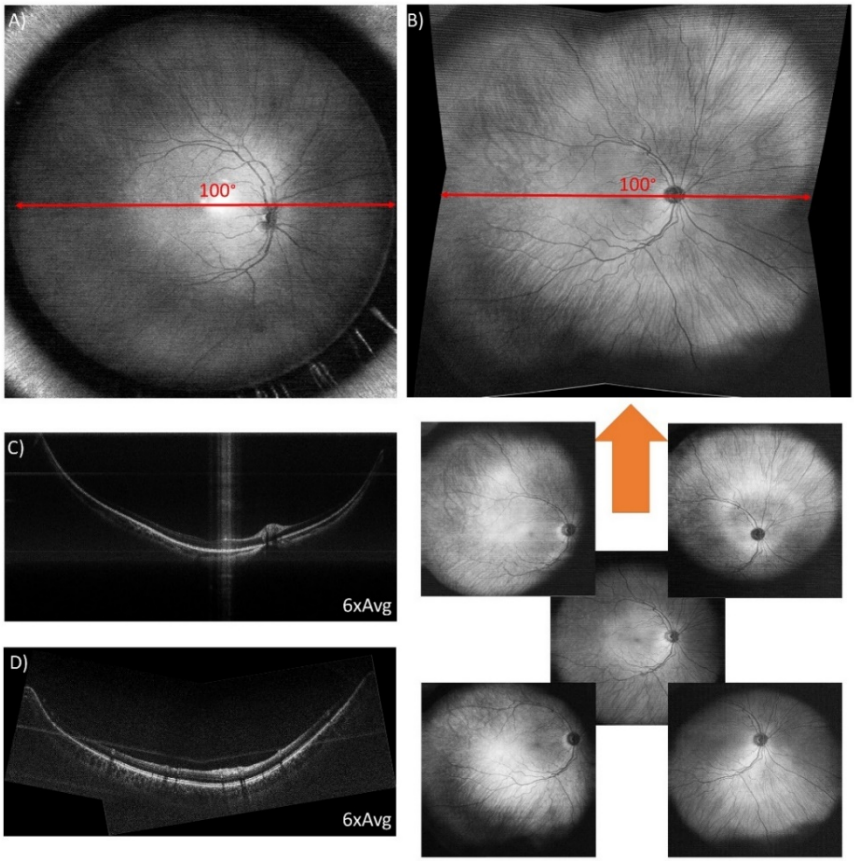

Fig. 9. Results of 100° ultra wide field in vivo retinal OCT imaging. A) En face projection from single volume imaging with the Volk SPXL. B) En face projections from 100° mosaicking with the stitched image (top) and the single volumes (bottom). C) Selected B-frame from 100° single volume imaging. A flythrough of all B-frames can be found in Media 3. The imaging depth is 6.8mm (in air). D) Selected B-frame for 100° mosaicking composed of two single B-frames. The total imaging depth is 4.8mm (in air).

#232125 - $15.00 USD Received 7 Jan 2015; revised 20 Feb 2015; accepted 23 Feb 2015; published 2 Apr 2015

Imaging was performed with non-dilated pupils only. Dilating was not necessary, as the lens would touch the cornea before the pivot point could be placed close enough to the posterior eye that clipping would occur at the pupil. Clipping occurred again only at the lens mount of L1. Shadowing of eyelashes became a significant challenge and multiple trials were necessary to get shadow-free images. An en face projection of the OCT data is displayed in Fig. 9(A) and a selected B-frame from this data set in subfigure C. All B-frames are presented in a flythrough in Media 3. The strong reflection in the center is due to the imperfect AR-coating on the Volk SPXL. The decrease of the signal towards the edges, which has already been observed and discussed for 85° imaging is even more pronounced. Again, the size of the bright center corresponds to the decrease of backcoupling efficiency at $\alpha \approx 20°$. The overall quality of the 100° ultra-widefield imaging can be considered marginally sufficient for any diagnostics and needs to be improved in the future.

4.3 100° mosaicking

We performed 100° imaging by mosaicking five 60° images to investigate whether a better image quality is achievable with this strategy. This few-tile mosaicking of only five, but comparably large data sets, in contrast to more common mosaicking of 10-20 tiles, has the advantage, that the patient does not have to refixate to the new target position too often. The total deadtime is kept low. The system was set back to the 85° imaging configuration and scanning protocol as described in section 0. However, the scanning amplitude of the galvo scanners was reduced to a 60°x60° field to avoid any clipping at the ophthalmic lens and thus reduce the percentage of A-scans per volume without information. We acquired five volumes – one in the center and one in each corner with an offset of ± 20°/ ± 20° in x/y-direction from the center to get a total coverage of 100°x100°. To achieve a rotation of the eye by the defined angle, the fixation target was projected at the corresponding positions. A slight translation was also necessary as the rotation point of the eye is not identical to the center of the entrance pupil. In post-processing, the en face projections of our images as well as selected B-frames were stitched with a panorama software for photography (PTGui, Photoshop).

Figure 9(B) and 9(D) display a stitched en face projection along with the single images and a B-frame, respectively. The single en face projections still feature slight shadowing in the edges which we attribute to clipping of the beam, now at the pupil. The overall image quality of the stitched image is much better than the one of the single volume 100° image. A systematic decrease of signal strength towards the edges for the stitched images is not visible, only in the single images. This indicates that the backscattering characteristics of the retina tissue should be nearly isotropic as the backscattering angle is the same as for the single volume imaging. Consequently optical aberrations should be the main cause for the angle dependent sensitivity fall-off. Here almost all aberrations are caused by the Volk lenses. As discussed before, this is underlined by the measurement of the angle dependent backcoupling efficiency which agrees roughly with the bright centers observed in the imaging results. As it is possible to achieve good quality images with mosaicing, improved free space optics with custom designed lenses should make at least the same quality in single volume imaging possible.

5. Summary and outlook

This paper investigates to what extend the FOV in retinal ultra-widefield OCT can be increased. We outline the numerous challenges related to this objective and discuss how they can be met. Detailed insight into the design considerations of our sample arm with focus on the choice of the necessary optics and the rest of our setup is given and the setup is characterized with respect to the challenges presented before. For the first time, we demonstrate single volume ultra-widefield imaging with up to 100° FOV and mosaicking with 100°x100° - in both cases with high definition dense isotropic sampling. We almost tripled the covered surface area compared to the standard 60° FOV of our previous MHz-OCT

#232125 - $15.00 USD Received 7 Jan 2015; revised 20 Feb 2015; accepted 23 Feb 2015; published 2 Apr 2015

results. Reasonable quality image data of 85° single volume OCT and 100° mosaicking is presented. These are the widest field of view OCT images with a dense sampling pattern to date. The signal decrease towards the edges can be explained for the most part. Our experiments suggest that the optical aberrations of our system are the main reason for this roll-off. A focal shift out of the imaging plane or angle dependent backscattering from the retina contribute only marginally. Here, only two healthy subjects were imaged with our ultra-widefield OCT setup. Therefore future studies with patients are required to determine which influence aberrations in the human eye have.

Based on our findings there are two major challenges remaining towards single volume high quality OCT with even larger FOVs. First, the optical design of the system: The optical aberrations of the sample arm need to be minimized. In future work the sample arm design needs to be optimized using appropriate ultra-widefield eye models [60]. Second, the image curvature over such a large FOV: This curvature either needs to be reduced by the optical design of the system or some active compensation like a rapidly length-adjustable reference arm or an optical or electronic frequency shifter. Alternatively, faster digitizer cards with multi-GHz sampling rates could increase the imaging range of MHz-OCT to a sufficient amount for even larger FOVs. Here, the high coherence length of our FDML laser was sufficient but also necessary, underlining the preference towards a long coherence length SS-OCT system rather than an SD-OCT. Based on our results we strongly believe that ~90° FOV OCT systems for clinical practice are possible and that such ultra-widefield OCT imaging will be highly beneficial for future clinical diagnosis.

Acknowledgments

We would like to acknowledge support from W. Zinth at the Ludwig-Maximilians-University Munich, A. Vogel at the University of Lübeck and the Munich Center for Advanced Photonics. Moreover we would like thank J.G. Fujimoto at MIT for fruitful discussions on the angle dependent sensitivity. This research was sponsored by the Emmy Noether program of the German Research Foundation (DFG – HU 1006/3-1) as well as by the European Union projects FUN-OCT (FP7 HEALTH, contract no. 201880) and FDML-Raman (FP7 ERC, contract no. 259158).

#232125 - $15.00 USD Received 7 Jan 2015; revised 20 Feb 2015; accepted 23 Feb 2015; published 2 Apr 2015